Sound & Vibration 2026, 60(6), 4615.
doi: https://doi.org/10.59400/sv4615

Article

Dynamic characterization and seismic performance evaluation of multi-span flyover bridge using ambient vibration testing and finite element modeling

Arief Kusbiantoro[1,*], Rini Kusumawardani[1], Endah Kanti Pangestuti[1], Faridh Rizal Rivandhani[1], Anindya Cirila[1], Sri Sutrisni[2], Noorsuhada Md Nor[3]

[1] Department of Civil Engineering, Faculty of Engineering, Universitas Negeri Semarang, Semarang 50229, Indonesia; rini.kusumawardani@mail.unnes.ac.id (RK); endahkp@mail.unnes.ac.id (EKP); faridhrizalrivandhani@gmail.com (FRR); aninrila03@students.unnes.ac.id (AC)

[2] Central Java Provincial Public Works and Highways Agency, Semarang 50144, Indonesia; tarimatrsshmieamla@gmail.com

[3] Faculty of Civil Engineering, Universiti Teknologi MARA Cawangan Pulau Pinang, Permatang Pauh 13500, Malaysia; ida_nsn@uitm.edu.my

*** Corresponding author:** Arief Kusbiantoro, arief_kusbiantoro@mail.unnes.ac.id

CITATION

Kusbiantoro A, Kusumawardani R, Pangestuti EK, et al. Dynamic characterization and seismic performance evaluation of multi-span flyover bridge using ambient vibration testing and finite element modeling. Sound & Vibration. 2026; 60(6): 4615. https://doi.org/10.59400/sv4615

ARTICLE INFO

Received: 3 July 2026
Revised: 26 July 2026
Accepted: 21 August 2026
Available online: 1 September 2026

Abstract: This study aims to evaluate the dynamic and seismic performance of an eight-span flyover bridge with a total length of 331 m using a combination of ambient vibration testing, finite element modeling, and non-linear seismic time-history analysis. The velocity data recorded during normal operation were evaluated using the Fast Fourier Transform to calculate the bridge's predominant natural frequency and validate a three-dimensional CSiBridge model. The natural frequencies obtained from the field measurement and numerical model were 3.670 Hz and 3.727 Hz, respectively, with a difference of 1.53%, which indicates reasonable agreement in the dominant frequency. The validated model was then analyzed by using artificial ground motions scaled to the required response spectrum with 5% damping. The seismic responses of the bridge piers were studied in terms of displacement, shear force, bending moment and axial force in the X and Y directions. The data suggest that the strongest seismic demands were focused at the middle piers, particularly at Pier 4. Furthermore, the comparison of the present bridge condition and the bridge with lead rubber bearings showed that the bearings reduced the displacement, shear force, and bending moment responses considerably. The results demonstrate that the model validation based on the vibration data provides a preliminary basis for subsequent seismic response analysis, and the lead rubber bearing can improve the seismic performance of multi-span flyover bridges efficiently.

Keywords: ambient vibration measurement; finite element model; seismic response; flyover bridge; lead rubber bearing; structural health monitoring

1. Introduction

Bridges are an essential component of transportation infrastructure, since they maintain the connectivity of road networks and enable the movement of people, goods, and services. In high seismic activity zones, bridges are vulnerable to vibrations from traffic and the environment, as well as earthquake pressures, ground displacement, impact loadings, scour, material degradation, and other multi-hazard impacts. These actions might cause large displacements, internal forces, degradation of stiffness, and accumulated damage of the bridge members, especially piers, bearings, foundations, and superstructures. Therefore, reliable evaluation of the dynamic characteristics and seismic performance of the bridge is vital to guarantee the structural safety, serviceability, and resilience.

Recent studies show that structural health monitoring, vibration-based identification, and digital twin-based evaluation provide useful ways to study the state and performance of civil infrastructure. Aroquipa et al. [1] developed a methodological framework that integrates structural health monitoring with digital-twin models for seismic assessment. They highlighted the importance of the integration of field measurement data with numerical simulations. Similarly, Reuland et al. [2] discussed a full-scale vibration-based monitoring case study and highlighted both the potential and remaining challenges of bridge structural health monitoring. Long-term monitoring has also been applied to multi-span highway bridges to evaluate seismic response and bearing conditions using wireless sensor networks [3]. These studies indicate that field-based dynamic measurement can provide important information for identifying structural characteristics and supporting seismic performance assessment.

Ambient vibration measurement has become an important non-destructive method for identifying the dynamic properties of bridges under operational conditions. This method allows for the identification of modal frequencies and vibration characteristics without disturbing the traffic flow and without any requirement for artificial excitation. Chen et al. [4] utilized ambient vibration measurements of a bridge superstructure to help in the assessment of scour at the foundations of a cable-stayed bridge. Zhan et al. [5] employed vibration measurement data and finite element model updating to assess the depth of scour at highway bridge piers. Wu et al. [6] investigated finite element model updating of a cable-stayed bridge based on vibration measurements and examined the variation of modal frequencies in monitoring applications. Furthermore, Chen et al. [7] showed that finite element models updated using vibration data can be applied to evaluate the necessity of tie-down devices in single-pylon cable-stayed bridges exposed to near-fault earthquakes. These results indicate that ambient vibration data play an important role in enhancing the reliability of numerical models and evaluating bridge performance.

Finite element modeling is frequently employed to evaluate bridge reactions to static, dynamic, and seismic stresses. However, the analytical models based on design assumptions, nominal material parameters, and simple boundary conditions might not accurately represent the true condition of the bridge. Such differences could be caused by numerous reasons in the field, such as construction tolerances, variation in the material characteristics, deterioration of the structure, flexibility of the support, modification of the support conditions, as well as environmental impacts. Therefore, the model should be updated based on measured dynamic properties to improve the reliability and accuracy of numerical simulations. Kusbiantoro et al. [8] studied the dynamic characteristics and finite element model of a single-span concrete girder bridge and structural health monitoring for identifying the dynamic characteristics and load rating factor of a multi-span prestressed concrete girder bridge. These studies show the importance of the combination of field data and finite element models for a reliable bridge assessment.

The seismic performance of bridge piers has received considerable attention because piers are among the most critical structural components during earthquakes. Various pier systems, loading cases, damage processes and strengthening methods have been investigated by many experimental and numerical investigations. Liang et al. [9] performed shaking table tests to study the effect of tri-directional stimulation and wave-passage effects on the seismic response of a long-span reinforced concrete deck-type arch bridge. Wang et al. [10] analyzed the seismic performance of external arched energy-dissipation links applied to precast segmental concrete-filled steel-tube bridge piers. Meanwhile, Al-Haaj et al. [11] studied the seismic behavior of unbonded post-tensioned precast hollow segmental bridge piers under biaxial lateral loading. Dong et al. [12] studied the influence of pile–soil interaction on the seismic response of self-centering rocking bridge piers by shaking table tests. Jia et al. [13] further researched pile-supported pier-superstructure systems under liquefaction-induced lateral spreading and highlighted the important roles of geotechnical conditions and soil-structure interaction in seismic analysis of bridges.

Previous research has also addressed the seismic and dynamic performance of reinforced concrete bridge piers under different damage and hazard conditions. Chen et al. [14] experimentally analyzed seismic responses of beam–column joints with and without fuse bars under lateral cyclic loading. Jiao et al. [15] performed shaking table tests of a curved bridge with variable pier heights. Shen et al. [16] studied seismic-resilient post-tensioned reinforced concrete bridge piers with improved bases. Tajali et al. [17, 18] applied a seismic assessment of a railway masonry arch bridge using a model updating technique based on sensors. Rashedi and Rahai [19] and Wang et al. [20] reviewed experimental and numerical advances in seismic evaluation of continuous RCC rigid-frame bridges. These studies collectively show the fact that the accurate seismic evaluation is dependent on structural configuration, pier detailing, boundary conditions, and the relation between experimental observations and numerical modelling.

In addition to earthquake excitation, bridge piers may also be affected by impact, blasting vibration, corrosion, and cumulative damage. Wang et al. [21] proposed intelligent identification of damage evolution in reinforced concrete bridge piers subjected to vessel collision and multi-hazard effects. Lin et al. [22] studied the impact behavior of hybrid FRP-concrete-steel double-skin tubular bridge piers. In the related works, Wang et al. [23] and Wang et al. [24] examined the dynamic properties of cast-in-place, precast, hollow, and ultra-high piers under longitudinal and repetitive impact loadings. Yao et al. [25] studied the behavior of viaduct piers on double-column dynamic under blast-induced vibration. In another work, Wu et al. [26] conducted an evaluation of the seismic performance of precast bridge piers with corrosion-damaged grouted sleeve connections. Zhou et al. [27] further studied cumulative impact damage in reinforced concrete piers based on modal frequencies. The research in general suggests that the behavior of the piers is affected by various dynamic challenges and that modal characteristics can be useful indicators for the identification of structural damage and deterioration.

Mitigation and strengthening strategies are essential to improve the safety and resilience of bridges. Saeed [28] investigated the simultaneous regulation of force and deformation in cable-arch-stayed bridges, while Hussain [29] investigated the use of polyurethane-cement material for strengthening concrete hollow-section girder bridges. Kamonna and Abd Al-Sada [30] evaluated the effect of bars near the surface on the structural behavior of reinforced concrete slabs. The investigations concentrate on strategies to reduce structural demands and to improve the performance of bridge elements using structural improvement strategies. Devices such as lead rubber bearings help reduce the transfer of loads from substructure to superstructure by enhancing the structural flexibility and dissipating the input energy for seismic applications. Therefore, these systems should lower the requirements of the displacement concentration, shear force, and bending moment in the critical bridge members. Aljidda et al. [31] investigated the flexural behavior of one-way reinforced concrete slabs strengthened using near-surface mounted (NSM) and externally bonded (EB) methods through experimental testing and finite element modeling. The results indicate that NSM-FRP can increase the ultimate load capacity by approximately 123% and enhance ductility, while the numerical results show good agreement with the experimental findings.

The literature study emphasizes the importance of field measurements, finite element modeling, seismic response analysis, and mitigation assessment as a comprehensive bridge performance evaluation process. However, more studies are still needed for the existing multi-span flyover bridges, especially those working under real traffic conditions and exposed to seismic pressure. The ambient vibration testing in combination with the finite element model validation provides a reasonable basis for the estimation of the real behavior of the bridges. Furthermore, comparing the existing bridge response with the response of a bridge equipped with seismic isolation devices can provide useful insight into the effectiveness of mitigation strategies.

The objective of this study is to evaluate the limited use of integrated field measurement, finite element assessment, and seismic-isolation evaluation on existing multi-span flyover bridges under operational conditions. The main contribution is the integrated implementation of ambient vibration data for the assessment of the numerical model, seismic time history analysis for the determination of the critical pier reactions, and a controlled comparison of configurations with and without lead rubber bearings. The paper also makes clear that the work offers a case-specific assessment approach, not a universal validation or code-compliance procedure.

2. Methodology

2.1. Object study

The bridge considered in this study is an important part of the 1,300-m-long road system and hence can carry a large amount of automobile traffic. The bridge comprises eight spans with a total length of 331 m, which enables the effective distribution of the loads and enhances the stability of the structure. The span width is determined to be 13.5 m to enable multi-lane traffic operations and to provide enough functional separation of the roadway. The bridge deck width is 11 m to facilitate the traffic movement and 0.3 m thick to maintain its structural integrity against dynamic stresses. The pier consists of a reinforced-concrete wall-type shaft with an approximate cross-section of 3.6 m × 1.8 m. The upper shaft is 5.2 m in the transverse direction and supports a pier head approximately 14.0 m long and 1.8 m wide. The overall pier height from the pile-cap top to the pier-head level is approximately 8.11 m. The pile cap is about 5.2 m × 3.2 m × 1.2 m and is supported by six piles. The superstructure is supported on a combination of fixed and movable bearing pads. The fixed bearings restrict vertical and the corresponding horizontal movements, while the movable bearings carry vertical loads but allow longitudinal movement due to temperature, creep, and shrinkage. In general, bearing rotations are modeled as released or represented by bearing stiffness. The pier shaft, pier head, and pile cap are modelled as monolithically connected. At bearing level, vertical translation is restrained at all supports, longitudinal translation is restrained at fixed bearings, and released or spring-supported at movable bearings. The bridge employs different material grades according to the function of each structural component. The reinforced-concrete deck slab, abutments, pier heads and pier shafts are designed to have a compressive strength of (f'c = 30) MPa. The precast U-girders are manufactured using a higher-strength concrete with (f'c = 50) MPa. The structural steel for the U-girders is classified as BJ 55 with an ultimate tensile strength (fu = 550) MPa and yield strength (fy = 410) MPa. Reinforcing bars are specified as U-32 grade steel. The prestressing is provided by seven-wire strands of 12.7 mm diameter. The superstructure is supported on elastomeric bearing pads that transfer vertical loads while accommodating limited rotation and horizontal movement.

2.2. Ambient vibration measurement

The dynamic response of the bridge under normal operating circumstances was investigated using ambient vibration measurements. Three velocity sensors made by Tokyo Sokushin were used. The sensor image is shown in **Figure 1**, and it is a compact cylindrical shape with a clearly defined directional arrow to guarantee the installation orientation. The frequency range of these instruments is 0.1 Hz to 70 Hz, and the high-sensitivity resolution is about 1.5×10^{-6} to 2×10^{-6} cm/s, which is ideal for the evaluation of substructure, microtremor analysis, and low-amplitude vibration assessment. Data of vibration were recorded by an SPC52 logger at a sampling frequency of 200 Hz over a 10-min interval, as shown in **Figure 2**, which is enough for modal analysis. This system allows for the immediate conversion of velocity data into time histories of acceleration and displacement. It runs with the PWave32 software suite that provides extensive signal processing and spectral analysis, including FFT spectra, H/V spectral ratios, response spectrum, and filtering operations. The sensor locations were optimized to provide accurate modal identification based on the first finite element (FE) model predictions of the mode shapes and natural frequencies. The sensors were positioned along the span, marked by the red arrows, at distances of 8.2 m, 16.4 m and 24.6 m, corresponding to locations at ¼ span, ½ span and ¾ span, as illustrated in **Figure 3**.

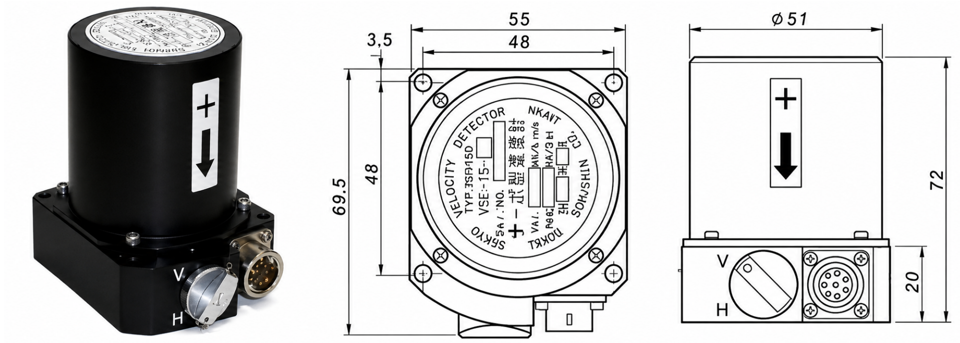

(a) Photo (b) Top View (c) Side View

Figure 1. Velocity-meter VSE-15D sensor.

Figure 2. Vibration measurement.

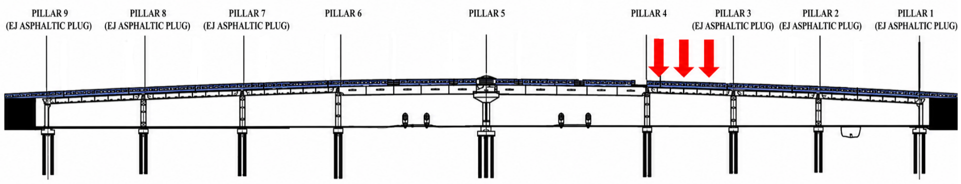

Figure 3. Placement of sensor.

2.3. Seismic load

In the seismic analysis, initially the earthquake load will be obtained in the form of a response spectrum shown in **Figure 4**, regarding the graph of the relationship between period parameters (seconds) and acceleration (g). This research uses the time history method analysis, so the spectrum response obtained must first be converted into Time History data and graphs. The conversion was carried out using SeismoSoft software, and the graph obtained can be seen in **Figure 5**. **Figure 4** presents an acceleration response spectrum, showing the relationship between spectral acceleration (Sa) and structural period (T). The horizontal axis is the period in seconds ranging from 0 to 10 s, while the vertical axis is the spectral acceleration in units of gravitational acceleration, g, with values of up to approximately 0.6 g. The spectrum exhibits a steep growth of spectral acceleration at very short periods, rising from about 0.18 g at (T = 0) s to a nearly flat peak plateau of about 0.48 g. This plateau is over the short-period range and represents the highest spectral demand in the record. Beyond this region, the spectral acceleration decreases gradually as the period increases. After about 0.5–0.7

s, a distinct reduction is observed, followed by a smoother and more gradual decay towards longer periods. **Figure 5** shows a time-history record of acceleration during 10 s. The time (in seconds) is shown on the horizontal axis, and the vertical axis refers to acceleration in units of gravitational acceleration, g. The recorded acceleration is oscillating about a near-zero baseline, which indicates an oscillatory ground-motion or vibration response. The signal is characterized by relatively low amplitudes at the beginning of the record and is followed by a more intense phase between approximately 1 and 4 s. In this interval, the acceleration oscillates rapidly and irregularly, with peaks of about +0.4 g and minimum values of about −0.4 g. After about 4 s, the amplitude gradually diminished indicating the decay of the intensity of movement. The waveform is much reduced and more regular from about 7 s onwards, eventually approaching near-zero acceleration at the end of the record.

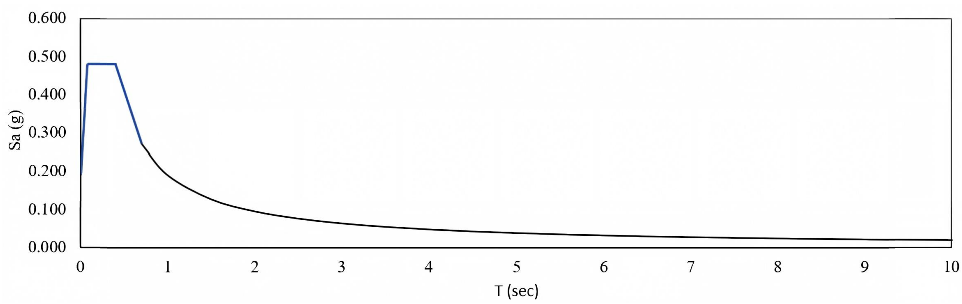

Figure 4. Response spectrum.

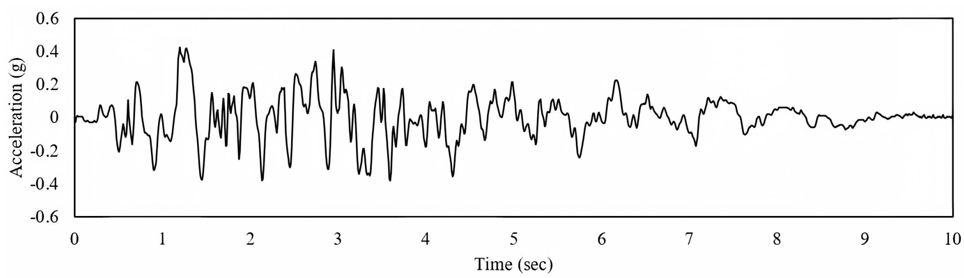

Figure 5. Time history.

The artificial acceleration time history was developed through a spectrum-compatible ground-motion generation procedure, in which the resulting accelerogram was adjusted to reproduce the prescribed target acceleration response spectrum. The target spectrum, presented in **Figure 4**, defines the variation of spectral acceleration (Sa) with structural period (T). In the present case, the target spectrum extends over a period range of 0–10 s. This range was adopted as the control interval for the spectrum-matching process in order to ensure that the generated time history would be compatible with the spectral ordinates relevant to both short-period and long-period structural response. A damping ratio of 5% of critical damping was adopted in the response spectrum calculation. This value is widely used in earthquake engineering as a representative damping level for conventional reinforced concrete and steel structural systems under seismic loading. The use of 5% damping allows the artificial accelerogram to be interpreted consistently with standard design response spectra, which are commonly defined for the same damping level. Therefore, the generated time history was matched to the target spectrum under the assumption that the structural response corresponds to a linear single-degree-of-freedom system with 5% viscous damping. The generated acceleration record, shown in **Figure 5**, has a total duration of 10 s. This time period corresponds to the time interval in which the artificial ground motion was synthesized and then adjusted. The selected duration is sufficient to include the main features of the motion, namely the initial build-up of acceleration, the strong-motion phase, and the final decay of the record. The time step of the accelerogram was taken as approximately 0.01 s. This small time increment provides adequate resolution for capturing the rapid changes in acceleration and is appropriate for numerical time-history analysis, particularly when the response of short-period structures is of interest. A scale factor of 1.0 was assumed during the generation and matching process. This implies that no additional amplitude scaling was applied to the final accelerogram after the matching procedure. In other words, the amplitude of the generated acceleration record was controlled directly by the target response spectrum. The resulting time history was therefore intended to reproduce the spectral acceleration ordinates of the target spectrum without subsequent modification of the acceleration values.

The spectrum matching process was assumed to be limited by a matching error of 5%. This parameter defines the acceptable difference between the response spectrum obtained from the generated accelerogram and the prescribed response spectrum. A smaller error limit generally gives a closer agreement with the target spectrum, but may require more iterations. It may introduce artificial characteristics into the time history. On the other hand, a larger error tolerance reduces the computational cost, but may lead to a less accurate spectral matching. For this study, a 5% error limit was considered acceptable as it provides an acceptable compromise between spectral accuracy and preservation of a realistic acceleration waveform. The maximum number of iterations was taken as 30. In the spectrum matching procedure, the accelerogram is iteratively modified until the calculated response spectrum meets the imposed error tolerance or the maximum number of iterations is reached. The 30 iterations used provide enough opportunity for convergence without allowing the acceleration record to be excessively modified. This parameter is important because excessive iterations may lead to a time history that matches the target spectrum numerically but contains unrealistic oscillatory features or non-physical characteristics. An envelope function was used to define the non-stationary amplitude modulation of the artificial accelerogram. The envelope controls the temporal distribution of acceleration amplitudes and ensures that the generated record resembles an earthquake-type ground motion rather than a stationary random signal. Based on the shape of the acceleration time history in **Figure 5**, the adopted envelope can be described as a trapezoidal or compound envelope consisting of three main stages. The first stage is the buildup phase, occurring from approximately 0 to 1 s, during which the amplitude of the acceleration increases slowly from a low initial value. The second stage is the strong-motion phase, which lasts approximately from 1 s to 4 s. The acceleration amplitudes in the strong-motion phase are relatively large, and the major energy content of the record is concentrated in this phase. The third stage is the decay phase. This phase lasts from about 4 s to 10 s, while the amplitudes of acceleration gradually decrease until the motion is almost zero. What is important about the use of this envelope is that it makes the artificial ground motion have a realistic temporal variation. Earthquake accelerograms are typically non-stationary, with energy not evenly distributed in time over the duration of the record. But they are characterized by an initial arrival of seismic waves, a period of intense shaking, and a gradual decrease in the amplitude of the motion. The adopted envelope function therefore provides a simplified but physically meaningful description of this behavior.

2.4. Lead rubber bearing

The bearing pads used in the flyover bridge consist of elastomeric rubber pads. For structural modelling purposes, the bridge bearing system was idealized as comprising pinned and roller supports. The bearing pad at the pinned support was modelled in CSiBridge by assigning release conditions to the translational and rotational degrees of freedom. All degrees of freedom were defined as fixed, except for rotation about the axis normal to the alignment line (R2), which was defined as free. In addition to pinned supports, the existing flyover bridge incorporates roller supports. The bearing pad at the roller support was modelled in CSiBridge by assigning release conditions to the translational and rotational degrees of freedom. All degrees of freedom were defined as fixed, except for translation along the alignment line (U3), which was defined as free. The stiffness in the U1 direction was specified as 4.69×10^6 kN/m, whereas the stiffnesses in the U2 and U3 directions were each specified as 5.07×10^6 kN/m. These values correspond to the vertical stiffness and effective stiffness parameters given in the LRB specifications. All rotational degrees of freedom were defined as free.

3. Results and discussion

3.1. Finite element model

In the analysis of earthquake-induced loads, the initial seismic input is obtained in the form of a response spectrum, which characterizes the dynamic behavior of the structure under ground motion. Based on this input, a three-dimensional finite element (FE) model of the flyover bridge is developed using CSiBridge to represent its structural configuration and dynamic characteristics. The complete bridge model is shown in **Figure 6**, illustrating the overall geometry and key structural components. No single universal mesh size is prescribed for bridge modelling in CSiBridge. In the analysis, the adopted mesh size is verified through a systematic mesh-convergence study with a difference of less than approximately 5% between two successive meshes. From the modal analysis of the bridge, the modal frequency of the bridge is 3.727 Hz.

3.2. Ambient vibration testing

The field measurements are used to identify the inherent frequencies of the structure and the associated ranges of vibration in June 2024. During the field measurement campaign, no meteorological and environmental data were evaluated. The data did not have detailed traffic operating characteristics such as approximate vehicle flow and vehicle classification. In addition, documentation concerning the calibration status of the velocity sensors was unavailable. Consequently, the possible influence of environmental and traffic variability on the measured structural response could not be evaluated and is acknowledged as a limitation of the study. **Figure 7** presents the velocity time histories recorded by three vibration sensors, identified as Sensor 1, Sensor 2, and Sensor 3. The horizontal axis indicates time in seconds up to around 550 s and the vertical axis is vibration velocity in cm/s. Each subplot presents the change in velocity over time at a different measurement point. In general, the three records show comparable waveform patterns, indicating that the sensors detected similar vibration events during the monitoring period. The velocity responses mainly fluctuate around zero with several transient pulses of different amplitudes. We can separate a number of different vibration events. Most notably, at the beginning of the record, between about 20 and 80 s, at about 160–180 s, around 225–260 s, around 315–325 s, and again approximately between 430 and 490 s. The largest responses of all these events are around 315–325 s, where the velocity amplitudes are about ±0.5 to ±0.7 cm/s depending on the sensor. Sensor 2 tends to show slightly higher peak amplitudes than Sensors 1 and 3, especially during the stronger bursts of vibration. The response of Sensor 3, however, often shows smaller amplitudes, but the response pattern is the same as the responses of the other sensors. The repeated presence of short-duration pulses with quite large amplitudes suggests that the recorded vibrations are transitory events and not continuous ones. The similarity in the three sensor recordings indicates spatial consistency in vibration response; nevertheless, the variations in amplitude can be attributed to the sensor location, coupling conditions, or wave propagation effects within the monitored structure or surrounding ground medium. Overall, the figure demonstrates that the vibration environment is dominated by discrete excitation events separated by intervals of relatively low background motion. Modal frequencies were identified by using the Fast Fourier Transform (FFT). **Figure 8** illustrates the frequency spectrum of the dynamic response measured, with amplitude plotted as a function of frequency (Hz), indicating that the system exhibits heightened sensitivity primarily at 3.670 Hz. This result only has a very small difference (1.53%) when compared to the frequency value from the vibration measurements. From the frequency comparison, it can be concluded that the FE model can reasonably capture the main dynamic characteristics of the bridge for subsequent simulations for seismic analysis.

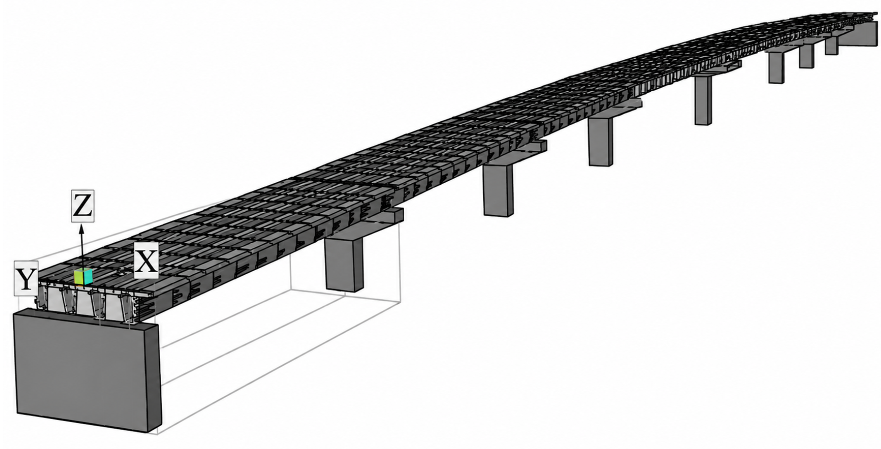

Figure 6. Three-dimensional finite element model of the flyover bridge.

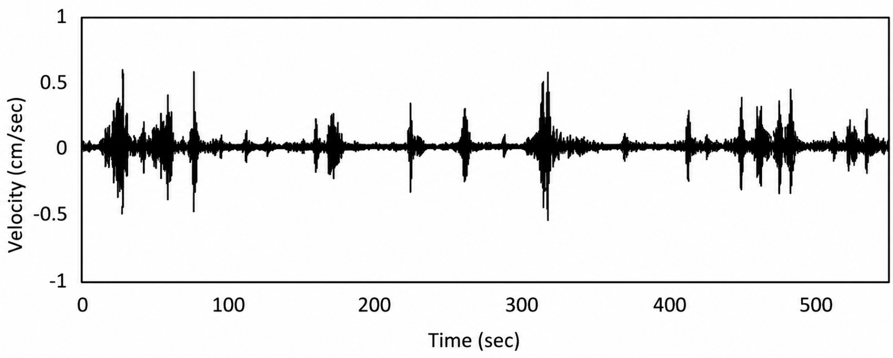

(a)

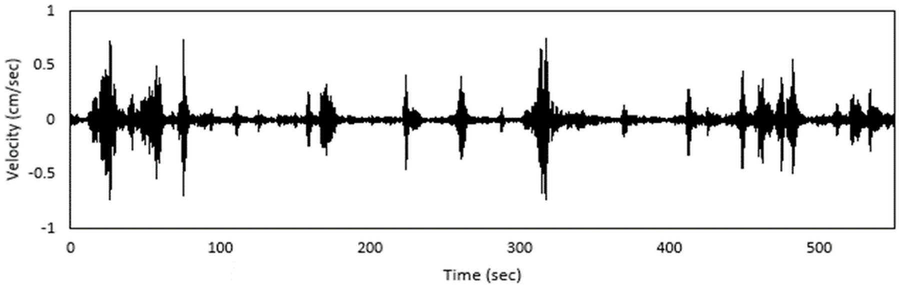

(b)

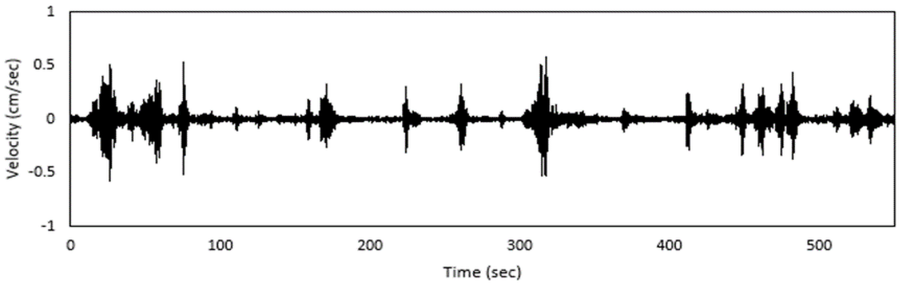

(c)

Figure 7. Velocity of vibration: **(a)** Sensor 1; **(b)** Sensor 2; **(c)** Sensor 3.

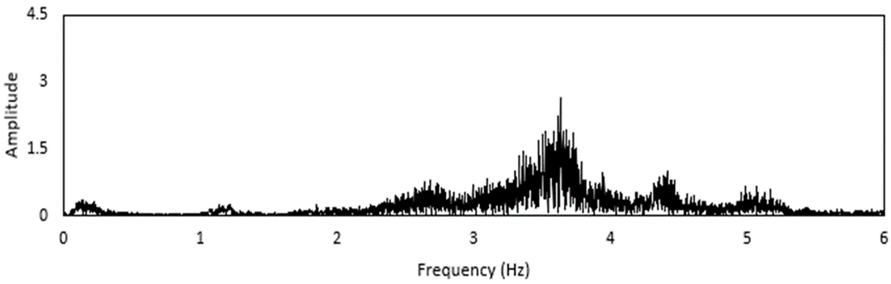

(a)

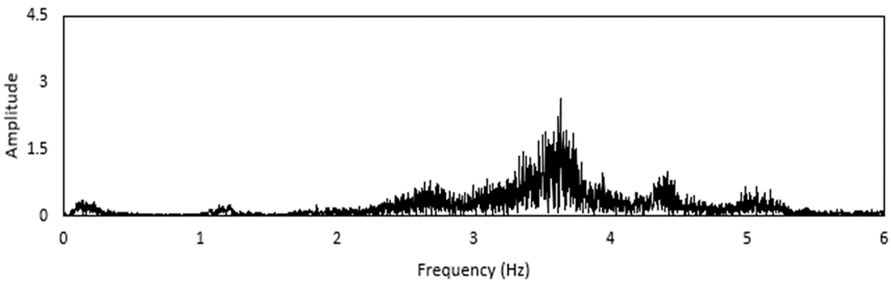

(b)

Figure 8. *Cont.*

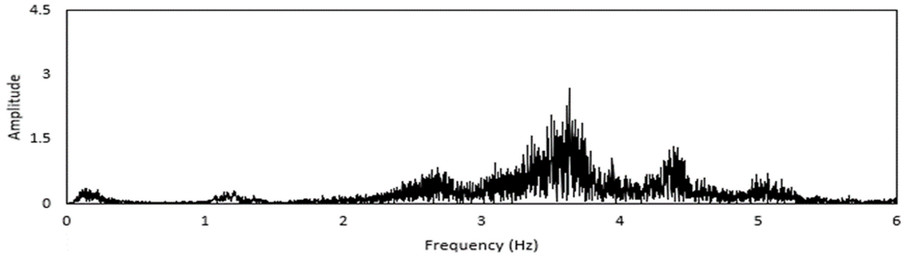

(c)

Figure 8. FFT: **(a)** Sensor 1; **(b)** Sensor 2; **(c)** Sensor 3.

Table 1 represents the displacements of the flyover bridge piers in the global X, Y, and Z directions under the seismic loading, with a special emphasis on load applications in the X and Y directions, respectively. The displacement components are reported in terms of U1, U2, and U3, corresponding to displacement components in directions X, Y, and Z, respectively, and all values are expressed in millimetres. When the earthquake load is applied in the X direction, the displacement response is generally dominated by the U1 components, which means the structural movement is in line with the direction of seismic excitation. The biggest U1 displacement is at Pier 4, which is −1.520 mm, indicating that this pier has the maximum lateral displacement in the X direction. The rest of the piers have lower values of U1 displacement, ranging from about 5.48×10^{-2} mm to -2.42×10^{-1} mm. Meanwhile, the displacement components of U2 and U3 are relatively minor, mainly in the order of 10^{-3} to 10^{-6} mm. This shows that the effects of transverse and vertical displacements are limited under the seismic excitation in the X direction. For the earthquake excitation in the Y direction, the displacement response is mainly controlled by the component U2, which corresponds to the displacement in the Y direction. The maximum displacement is found at Pier 4 with a U2 value of -3.57×10^{1} mm. Then, Pier 3 and Pier 5 present U2 values of -2.14×10^{1} mm and -2.07×10^{1} mm, respectively. These results show that the center piers are significantly more sensitive to Y-direction earthquake loads. The components U1 and U3 under the Y-direction excitation are relatively tiny, generally in the order of 10^{-2} to 10^{-6} mm, which indicates that the reaction is substantially concentrated in the direction of the applied seismic action.

Table 1. Displacement.

Pier	Due to an earthquake in the X direction			Due to an earthquake in the Y direction		
	U1 Displacement X (mm)	U2 Displacement Y (mm)	U3 Displacement Z (mm)	U1 Displacement X (mm)	U2 Displacement Y (mm)	U3 Displacement Z (mm)
1	5.48×10^{-2}	-9.14×10^{-6}	-4.44×10^{-4}	-2.05×10^{-4}	8.02×10^{-2}	-1.67×10^{-6}
2	-8.55×10^{-2}	3.67×10^{-4}	4.16×10^{-4}	-3.19×10^{-4}	−3.201	1.49×10^{-6}
3	-2.42×10^{-1}	2.47×10^{-3}	-4.66×10^{-3}	-1.19×10^{-3}	-2.14×10^{1}	1.96×10^{-5}
4	−1.520	-4.12×10^{-3}	-2.99×10^{-3}	-1.09×10^{-2}	-3.57×10^{1}	-1.22×10^{-5}
5	1.67×10^{-1}	2.39×10^{-3}	6.33×10^{-3}	-7.25×10^{-4}	-2.07×10^{1}	-2.18×10^{-5}
6	9.49×10^{-2}	6.79×10^{-4}	-8.14×10^{-4}	-3.691×10^{-4}	−5.917	2.23×10^{-6}
7	6.15×10^{-2}	-5.88×10^{-5}	2.76×10^{-4}	-2.61×10^{-4}	5.09×10^{-1}	-5.88×10^{-7}

Moreover, **Table 2** presents the shear force response of all bridge piers under seismic excitation applied in the X and Y directions. The results are reported for two shear components, namely Shear 2-2 in the Y direction and Shear 3-3 in the X direction.

Under earthquake loading in the X direction, the dominant shear response occurs in the Shear 3-3 component, which corresponds to shear force in the X direction. The biggest value is found at Pier 4 with the shear force of -6.81×10^2 kN, which means that this pier is exposed to the greatest shear demand in the X-direction seismic excitation. Also, at Pier 3 and Pier 5, major Shear 3-3 responses are discovered with values of -7.66×10^1 kN and 5.04×10^1 kN, respectively. In contrast, the Shear 2-2 response for X-direction excitation is comparatively modest, usually below 1 kN, suggesting little shear transfer in the transverse Y direction. The response to the earthquake load in the Y direction is predominantly dominated by the Shear 2-2 component. The maximum shear force occurs at Pier 4 with a value of 8.63×10^3 kN, followed by Pier 3 and Pier 5 with 6.61×10^3 kN and 5.39×10^3 kN, respectively. It is observed that the shear demands of the central piers are significantly higher in the case of seismic stimulation in the Y direction. Meanwhile, the Shear 3-3 component under the Y-direction excitation is quite tiny, ranging from -8.40×10^{-2} kN to -4.91×10^{-1} kN. In general, the shear force response is strongly dependent on the direction of the earthquake excitation. Shear forces in the X-related Shear 3-3 component are predominantly caused by loading in the X direction due to seismic activity, whereas loading in the Y direction causes considerably greater shear forces in the Y-related Shear 2-2 component. Pier 4 regularly records the largest shear response for both seismic loading directions, which indicates that Pier 4 is the most significant pier toward seismic shear demand and requires special attention in structural evaluation and seismic design assessment.

Table 2. Shear force under seismic.

Pier	Due to an earthquake in the X direction		Due to an earthquake in the Y direction	
	Shear 2-2 (Y) (kN)	Shear 3-3 (X) (kN)	Shear 2-2 (Y) (kN)	Shear 3-3 (X) (kN)
1	-2.83×10^{-4}	-2.88×10^{1}	1.58×10^{2}	-1.08×10^{-1}
2	-2.04×10^{-1}	-2.26×10^{1}	1.77×10^{3}	-8.40×10^{-2}
3	7.84×10^{-1}	-7.66×10^{1}	6.61×10^{3}	-3.27×10^{-1}
4	1.04×10^{-1}	-6.81×10^{2}	8.63×10^{3}	-4.91×10^{-1}
5	-6.46×10^{-1}	5.04×10^{1}	5.39×10^{3}	-2.27×10^{-1}
6	-3.94×10^{-1}	3.22×10^{1}	3.44×10^{3}	-1.09×10^{-1}
7	7.50×10^{-2}	4.40×10^{1}	-6.55×10^{2}	-2.07×10^{-1}

Table 3 presents the bending moment response of seven bridge piers under seismic excitation applied in the X and Y directions. The moment components are expressed as Moment 2-2 in the Y direction and Moment 3-3 in the X direction. Under earthquake loading in the X direction, the dominant response is observed in the Moment 2-2 component. Pier 4 shows the largest moment response of -7.06×10^3, which indicates the pier is under the highest bending demand during X-direction seismic stimulation. All the remaining piers have substantially lower Moment 2-2 values between about -1.84×10^2 and 3.30×10^2. By comparison, the Moment 3-3 component of the X-direction excitation is rather small, where the greatest value also occurs at Pier 4, 1.69×10^1. Then Pier 3 and Pier 5 follow with values of -1.46×10^1 and -1.31×10^1, respectively. The structural response to earthquake loading in the Y direction is mostly influenced by the component of Moment 3-3. The greatest moment was observed for Pier 4 with 1.46×10^5, followed by Pier 3 and 5 with 1.26×10^5 and

1.13×10^5, respectively. The results reveal that the center piers are more affected by the bending effects under the seismic stimulation in the Y direction. Meanwhile, the Moment 2-2 component under Y-direction excitation is quite small; most values are below 3 in magnitude, except for Pier 4, where the value is up to -5.09×10^1. The results indicate that the moment response of the bridge piers is significantly influenced by the seismic loading direction. Earthquake excitation in the X direction primarily produces bending about the 2-2 axis, while that in the Y direction provides much greater bending about the 3-3 axis. Pier 4 consistently shows the most critical response, indicating that it is the most vulnerable pier in terms of seismic bending demand and should be given particular attention in structural assessment and seismic design verification.

Table 3. Moment under seismic.

Pier	Due to an earthquake in the X direction		Due to an earthquake in the Y direction	
	Moment 2-2 (Y) (kNm)	**Moment 3-3 (X) (kNm)**	**Moment 2-2 (Y) (kNm)**	**Moment 3-3 (X) (kNm)**
1	-1.64×10^2	-7.73×10^{-2}	-6.17×10^{-1}	-6.89×10^2
2	-1.84×10^2	-2.70	-6.84×10^{-1}	2.35×10^4
3	-5.02×10^1	-1.46×10^1	-2.25	1.26×10^5
4	-7.06×10^3	1.69×10^1	-5.09×10^1	1.46×10^5
5	3.30×10^2	-1.31×10^1	-1.46	1.13×10^5
6	2.08×10^2	-4.58	-7.71×10^{-1}	3.99×10^4
7	2.02×10^2	5.52×10^{-1}	-8.96×10^{-1}	-4.78×10^3

Table 4 presents the axial force response of seven bridge piers under seismic excitation in the X and Y directions. Under seismic excitation in the X direction, the axial force response is relatively significant compared with that produced by Y-direction excitation. The axial force of maximum positive value is 1.39×10^2 kN at Pier 5, and the axial force of maximum negative value is -1.07×10^2 kN at Pier 3. Also, Pier 4 has a quite large negative axial force of -8.78×10^1 kN. These results show that the earthquake excitation in the X direction shows significant variation in the axial forces of the piers. Both tensile and compressive responses are observed depending on the pier location and structural interaction. By comparison, the axial forces induced by Y-direction earthquake loading are much smaller. The values vary from -4.78×10^{-1} kN at Pier 5 to 4.51×10^{-1} kN at Pier 3. This suggests that seismic excitation in the Y direction has only a limited effect on the axial force response of the piers when compared with X-direction excitation. The relatively small values also indicate that axial effects under Y-direction loading are negligible compared with the corresponding response in the X direction. Overall, the results indicate that the axial force response is very dependent on the direction of seismic excitation. Earthquake loading in the X direction results in significantly higher axial forces, especially in Piers 3–5, while earthquake loading in the Y direction results in only small changes in axial forces. Pier 5 experiences the highest positive axial force, while Pier 3 records the highest negative axial force, indicating that these piers should be considered important locations in evaluating axial demand under seismic loading.

Table 4. Axial force under seismic.

Pier	Axial (kN)	
	X direction	Y direction
1	-1.32×10^1	-5.01×10^{-2}
2	1.07×10^1	3.80×10^{-2}
3	-1.07×10^2	4.51×10^{-1}
4	-8.78×10^1	-3.59×10^{-1}
5	1.39×10^2	-4.78×10^{-1}
6	-1.95×10^1	5.30×10^{-2}
7	7.86	-1.70×10^{-2}

Figures 9–11 present a comparative structural response analysis between the bridge system without and equipped with lead rubber bearings (LRB), which were analyzed using the same seismic input and modeling assumptions. Three key response parameters are shown: displacement, shear force, and bending moment along the bridge span. Overall, the results indicate that the application of LRB significantly reduces the structural demand compared with the existing condition. In **Figure 9**, the displacement profile shows that both systems experience maximum displacement near the mid-span under lateral or dynamic loading. However, the displacement response of the LRB system is consistently smaller than that of the present bridge structure. The maximum displacement of the present bridge is around 1.0×10^{-2} m while the maximum displacement of the bridge with LRB is only approximately 6.0×10^{-3} m. This reduction indicates that LRB can successfully prevent excessive deformation by increasing structural flexibility and energy dissipation under loading. **Figure 10** shows a remarkable reduction in internal forces in the shear force distribution after LRB application. The present construction produces relatively strong shear forces, in particular in the support areas, up to 2.5×10^3 kN. Meanwhile, the LRB system leads to a lower and more uniform distribution of shear force, with the values not going above 7.0×10^2 kN in general. This implies that the LRB system limits the lateral forces transferred from the superstructure to the substructure. Accordingly, the bearing alleviates the seismic or dynamic shear demands on the bridge piers, abutments, and foundations. The bending moment distribution along the span is shown in **Figure 11**. The bending moments of the existing bridge are much bigger, which is consistent with the results of the displacement and shear force, with the maximum value being about 2.2×10^4 kN·m near the mid-span region. On the other hand, the maximal moment of the LRB system is substantially smaller, at 7.0×10^3 kN·m. This reduction depicts that the utilization of LRB could decrease the flexural demand of the bridge deck as well as its supporting structural elements. The LRB model also gives a smoother bending moment distribution, which means a more controlled and stable structural response. The results suggest the effectiveness of lead rubber bearings in improving the bridge performance by reducing the displacement, shear force, and bending moment demands. The LRB as an isolation mechanism collects and dissipates a portion of the input energy, thereby reducing the forces transmitted to the main structural elements. The bridge with LRB has a more desirable reaction in comparison to the existing bridge condition, especially for the reduction of internal forces. Thus, LRB implementation can be considered as an efficient structural mitigation approach to enhance bridge safety

and resilience, particularly under seismic or dynamic loading situations.

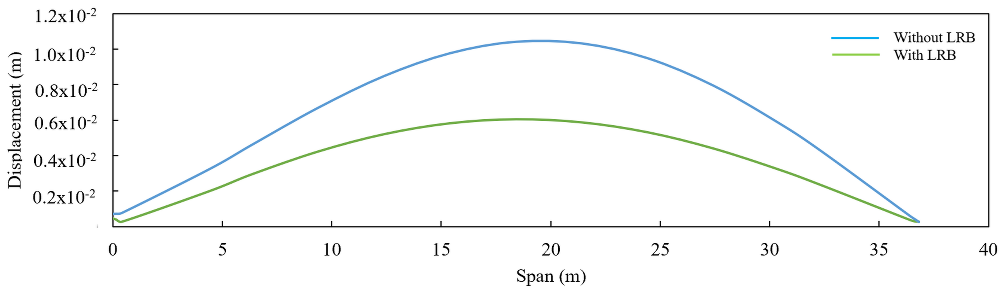

Figure 9. Displacement.

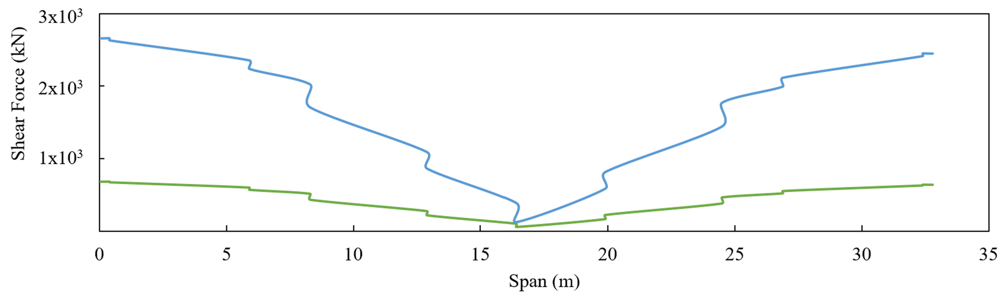

Figure 10. Shear force.

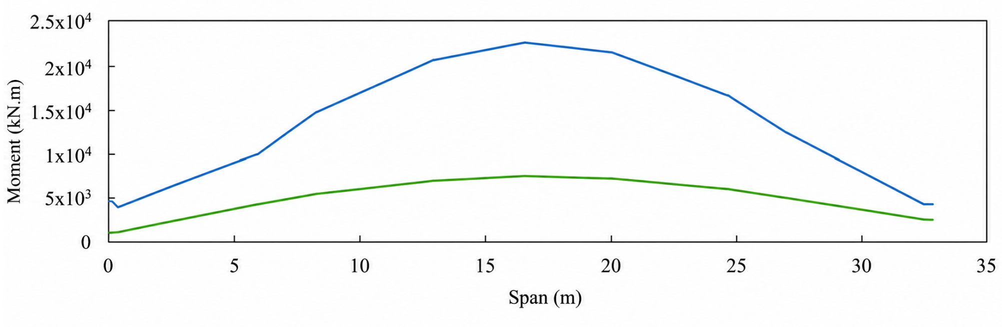

Figure 11. Moment.

4. Conclusion

The dynamic characteristics and seismic performance of a multi-span flyover bridge were studied using ambient vibration measurement, finite element modelling and time-history seismic analysis. Field vibration testing was successfully used to identify the major dynamic response of the bridge in operational conditions. The natural frequency observed was 3.670 Hz according to Fast Fourier Transform analysis. The modal frequency was 3.727 Hz using a finite element model. The difference between measured and numerical frequencies was only 1.53%. This indicates that the created finite element model can reasonably capture the main dynamic characteristics of the bridge and may be used for further investigation of seismic response.

The seismic analysis showed that the bridge response is strongly affected by the direction of earthquake excitation. Under X-direction seismic loading, the dominant displacement, shear force, and bending moment responses occurred mainly in the corresponding structural components associated with the direction of excitation. Under

Y-direction seismic loading, substantially larger lateral displacement, shear force, and bending moment demands were observed, especially at the central piers. Regarding the piers analyzed, Pier 4 responded most critically compared to the other piers relating to displacement, shear force, and bending moment. This result indicates that Pier 4 is the most vulnerable element for the given seismic loading circumstances, requiring special attention in the seismic assessment, reinforcing design and maintenance planning.

The axial force response was also affected by the direction of seismic excitation. The seismic loading in the X direction produced larger axial force variations than the loading in Y direction. The maximum positive axial force was at Pier 5, while the maximum negative axial force was at Pier 3. These results demonstrate that the seismic demands are not evenly distributed along the bridge and are influenced by pier position, structural continuity and excitation direction.

The comparison of the existing bridge with the bridge constructed with lead rubber bearings shows that seismic isolation can increase the structural performance significantly. The implementation of the lead rubber bearings decreased the displacement, shear force and bending moment responses along the bridge span. The isolated system produced smoother and lower internal force distributions, suggesting the bearings are effective in energy dissipation from seismic response and in reducing lateral force transmission to the bridge substructure. Therefore, the use of lead rubber bearings can be considered as an indicator of the relative efficiency of the LRB structure for the bridge and loading instance examined. For future research, a detailed comparison with various bearing systems such as elastomeric, friction-pendulum and high-damping rubber bearings should be carried out.

The results generally confirm that the combination of ambient vibration testing and finite element model validation provides a reliable basis for the seismic assessment of bridge structures. The validated model allows for more accurate prediction of seismic demand and assists in evaluating structural improvement methods. Future research may extend this work to address soil-structure interaction, bearing nonlinearity, numerous earthquake records, and long-term vibration monitoring to further increase the reliability of the bridge seismic performance assessment.

Author contributions: AK and RK conceived this research and designed the study; AK, RK, FRR, AC, SS, EKP and NMN participated in the field investigations and interpretations of the data; AK and RK wrote the paper and participated in the associated revisions. All authors read and approved the final manuscript.

Funding: This work was funded by the Research and Community Service Affairs, Universitas Negeri Semarang, with contract number 139.03.2.693449/2026.

Institutional review board statement: Not applicable.

Informed consent statement: Not applicable.

Data availability statement: No new data were created or analyzed in this study. Data sharing is not applicable to this article.

Acknowledgement: The authors would like to sincerely thank the technical staff and research assistants for their valuable assistance during the field measurements, data collection, and experimental work. Their support and cooperation were greatly appreciated and contributed significantly to the completion of this research.

Conflict of interest: The authors declare no conflict of interest.

AI use statement: During the preparation of this work, the authors used ChatGPT (OpenAI) for language editing, improving clarity and readability, and assisting with grammatical refinement of the manuscript. The authors subsequently reviewed and edited the content as necessary and take full responsibility for the final content of the published article.

References

1. Aroquipa H, Hurtado A, Angel C. Methodological framework for integrating structural health monitoring and digital-twin models for seismic assessment of heritage buildings: Case study of Basilica Maria Auxiliadora, Lima, Peru. Structures. 2025; 80: 110115. doi: 10.1016/j.istruc.2025.110115
2. Reuland Y, Garcia-Ramonda L, Martakis P, et al. A full-scale case study of vibration-based structural health monitoring of bridges: Prospects and open challenges. Ce/Papers. 2023; 6(5): 329–336. doi: 10.1002/cepa.2001
3. Siringoringo DM, Fujino Y, Suzuki M. Long-term continuous seismic monitoring of multi-span highway bridge and evaluation of bearing condition by wireless sensor network. Engineering Structures. 2023; 276: 115372. doi: 10.1016/j.engstruct.2022.115372
4. Chen CC, Wu WH, Shih F, et al. Scour evaluation for foundation of a cable-stayed bridge based on ambient vibration measurements of superstructure. NDT & E International. 2014; 66: 16–27. doi: 10.1016/j.ndteint.2014.04.005
5. Zhan J, Wang Y, Zhang F, et al. Scour depth evaluation of highway bridge piers using vibration measurements and finite element model updating. Engineering Structures. 2022; 253: 113815. doi: 10.1016/j.engstruct.2021.113815
6. Wu WH, Chen CC, Kusbiantoro A, et al. Finite element model of a cable-stayed bridge updated with vibration measurements and its application to investigate the variation of modal frequencies in monitoring. Structure and Infrastructure Engineering. 2024; 20(5): 760–770. doi: 10.1080/15732479.2022.2132517
7. Chen CC, Wu WH, Kusbiantoro A, et al. Necessity investigation of tie-down devices for single-pylon cable-stayed bridges to resist near-fault earthquakes with finite element models updated by vibration measurements. Structure and Infrastructure Engineering. 2025; 21(4): 563–578. doi: 10.1080/15732479.2023.2225053
8. Kusbiantoro A, Kusumawardani R, Wirawan AB, et al. Assessment of dynamic properties and finite element model on single-span concrete girder bridge. International Journal of Engineering. 2026; 39(3): 727–738. doi: 10.5829/ije.2026.39.03c.13
9. Liang X, Du C, Li ZX. Influence of tri-directional excitation and wave-passage effect on seismic response of a long-span reinforced concrete deck-type arch bridge: Shake table test. Soil Dynamics and Earthquake Engineering. 2025; 198: 109552. doi: 10.1016/j.soildyn.2025.109552
10. Wang C, Liu R, Fu L, et al. Seismic performance investigation of external arched energy-dissipation links in precast segmental concrete-filled steel-tube bridge piers. Structures. 2025; 81: 110172. doi: 10.1016/j.istruc.2025.110172
11. Al-Haaj M, Wang S, Al-Shaebi R, et al. Seismic performance of unbonded posttensioned precast hollow segmental bridge piers under biaxial lateral loading. Structures. 2025; 76: 108985. doi: 10.1016/j.istruc.2025.108985
12. Dong H, Fan G, Huang J, et al. Shaking table tests of the influence of pile–soil interaction on seismic responses of self-centering rocking bridge piers. Soil Dynamics and Earthquake Engineering. 2026; 200(Part B): 109837. doi: 10.1016/j.soildyn.2025.109837
13. Jia K, El Naggar MH, Xu C, et al. Seismic behavior of piles-supported pier–superstructure to liquefaction-induced lateral spreading considering variability of soil permeability. Canadian Geotechnical Journal. 2025; 62: 1–22. doi: 10.1139/cgj-2023-0749
14. Chen P, Pan J, Hu F, et al. Experimental investigation on earthquake-resilient steel beam-to-column joints with replaceable buckling-restrained fuses. Journal of Constructional Steel Research. 2022; 196: 107413. doi: 10.1016/j.jcsr.2022.107413

15. Jiao C, Wang K, Ma H, et al. Shaking table test study on seismic performance of a curved bridge with concave island-type variable pier height. Soil Dynamics and Earthquake Engineering. 2025; 199: 109702. doi: 10.1016/j.soildyn.2025.109702
16. Shen Y, Freddi F, Li Y, et al. Shaking table tests of seismic-resilient post-tensioned reinforced concrete bridge piers with enhanced bases. Engineering Structures. 2024; 305: 117690. doi: 10.1016/j.engstruct.2024.117690
17. Tajali M, Ataei S, Miri A, et al. Seismic assessment of a railway masonry arch bridge using sensor-based model updating. Proceedings of the Institution of Civil Engineers – Bridge Engineering. 2025; 178(1): 3–14. doi: 10.1680/jbren.22.00019
18. Ni Z, Zhan J, Xu X, et al. A rapid damage identification method for highway bridge double-column piers based on longitudinal dynamic stiffness. Engineering Failure Analysis. 2025; 182(Part C): 110192. doi: 10.1016/j.engfailanal.2025.110192
19. Rashedi SH, Rahai A. Experimental and numerical advances in seismic assessment of continuous RC rigid-frame bridges: A review. Results in Engineering. 2025; 26: 105656. doi: 10.1016/j.rineng.2025.105656
20. Wang M, Yin J, Xiong C, et al. Dynamic monitoring and characteristic analysis of a long-span operational bridge from high-rate sensor responses using the RAAVMD approach. Measurement. 2025; 244: 116498. doi: 10.1016/j.measurement.2024.116498
21. Wang W, Wang S, Fu J. Intelligent identification of the evolution process of damage on RC bridge piers under vessel collision considering multi-hazards. Ocean Engineering. 2025; 322: 120434. doi: 10.1016/j.oceaneng.2025.120434
22. Lin S, Zhang S, Zhang B, et al. Impact response of hybrid FRP-concrete-steel double-skin tubular bridge piers with fixed-simply supported boundary conditions: Experimental study and FE analysis. Structures. 2025; 75: 108730. doi: 10.1016/j.istruc.2025.108730
23. Wang J, Xu W, Wang J, et al. Experimental and numerical investigation on the dynamic performance of cast-in-place and precast hollow ultra-high piers under longitudinal impact. Thin-Walled Structures. 2025; 208: 112850. doi: 10.1016/j.tws.2024.112850
24. Wang J, Xu W, Wang J, et al. Experimental and numerical investigation on the dynamic response of RC ultra-high piers under multiple impacts. Structures. 2025; 75: 108855. doi: 10.1016/j.istruc.2025.108855
25. Yao Y, Zhu B, Jiang N, et al. Experimental study on the dynamic response of a double-column viaduct pier under the action of blasting vibration. Structures. 2025; 76: 108939. doi: 10.1016/j.istruc.2025.108939
26. Wu X, Yuan W, Guo A. Experimental study on seismic performance of precast bridge piers with corrosion-damaged grouted sleeve connections. Structures. 2025; 75: 108699. doi: 10.1016/j.istruc.2025.108699
27. Zhou X, Zhou M, Gao Y, et al. An evaluation study on the cumulative impact damages of reinforced concrete piers based on modal frequencies. Engineering Failure Analysis. 2021; 119: 104983. doi: 10.1016/j.engfailanal.2020.104983
28. Saeed MN. Simultaneous force and deformation control of cable arch stayed bridges. Kufa Journal of Engineering. 2019; 10(4): 66–75. doi: 10.30572/2018/KJE/100406
29. Hussain HK. Strengthening concrete hollow-section girder bridge using polyurethane–cement material (Part B). Kufa Journal of Engineering. 2018; 9(1): 23–41. doi: 10.30572/2018/KJE/090102
30. Kamonna HH, Abd Al-Sada DJ. Effect of near-surface mounted bars on the structural behavior of one-way RC slab. Kufa Journal of Engineering. 2021; 12(3): 12–30. doi: 10.30572/2018/kje/120302
31. Aljidda O, El Refai A, Alnahhal W. Experimental and numerical investigation of the flexural behavior of one-way RC slabs strengthened with near-surface mounted and externally bonded systems. Construction and Building Materials. 2024; 421: 135709. doi: 10.1016/j.conbuildmat.2024.135709